Journal of the Physical Society of Japan **88**, 094709 (2019)
https://doi.org/10.7566/JPSJ.88.094709

The Complex Electronic Phase Diagram of Single-Crystalline R_2PdSi_3 (R = Ho, Dy) Studied by Thermal Expansion and Magnetostriction

Liran Wang[1]*, Binh Tran[1], Mingquan He[2], Christoph Meingast[2], Mahmoud Abdel-Hafiez[3,4]†, Chongde Cao[5], Holger Bitterlich[6], Wolfgang Löser[6], and Rüdiger Klingeler[1]‡

[1]*Kirchhoff Institute of Physics, Heidelberg University, INF 227, 69120 Heidelberg, Germany*
[2]*Institute for Solid State Physics, Karlsruhe Institute of Technology, 76021 Karlsruhe, Germany*
[3]*Physikalisches Institut, Goethe-Universität, 60323, Frankfurt am Main, Germany*
[4]*Faculty of Science, Physics Department, Fayoum University, 63514 Fayoum, Egypt*
[5]*Department of Applied Physics, Northwestern Polytechnical University, Xi'an 710072, P. R. China*
[6]*Leibniz Institute for Solid State and Materials Research IFW Dresden, Helmholtzstr. 20, 01069 Dresden, Germany*

(Received June 6, 2019; accepted July 12, 2019; published online August 20, 2019)

Thermal expansion and magnetostriction of single-crystalline R_2PdSi_3 (R = Ho, Dy) have been investigated by means of high-precision capacitance dilatometry and by specific heat studies. Pronounced anomalies in the uniaxial thermal expansion coefficients α_a and α_c and in the specific heat c_p mark the onset of long-range antiferromagnetic (AFM) order at $T_N = 7.8(3)$ K (R = Ho) and $T_N = 7.9(3)$ K (R = Dy). The different nature of the ground states in both materials is concluded from opposite signs of the thermal expansion anomalies, i.e., opposite uniaxial pressure dependencies. In both materials, there are Schottky-like entropy and anisotropic length changes which are attributed to crystal field effects and reorientation of the easy magnetic axes. The low-temperature magnetic phase diagrams and the magnetostriction data imply an interplay of single-ion effects and magnetic exchange interaction. Even small magnetic fields yield ferrimagnetic phases via yet unknown intermediate antiferromagnetic (Dy_2PdSi_3) and ferrimagnetic (Ho_2PdSi_3) phases.

1. Introduction

Ternary rare earth intermetallic compounds R_2TSi_3 (R = rare earth, T = transition metals) have been subject to intensive research over the last decades as they exhibit a variety of phenomena such as superconductivity,[1)] spin-glass,[2)] or ferromagnetic behaviour,[3)] giant magnetoresistance (GMR),[4)] or Kondo effect.[5)] Recently, the materials have been identified as promising candidates for magnetocaloric applications and a giant reversible magnetocaloric effect has been recently reported in Ho_2PdSi_3.[6,7)] Most of the known members of this class crystallize in a hexagonal AlB_2-type derived structure (space group $P6/mmm$).[8)] As for R_2PdSi_3 (R = Ho, Dy) compounds, neutron diffraction reveals that the R ions occupy the Al-sites whereas the Pd and Si atoms were assumed to be statistically distributed over the B-sites.[9)] X-Ray diffraction measurements on single-crystals, however, suggest the existence of a superstructure in the R_2PdSi_3 (R = Gd, Tb, Dy, Ho, Er, Tm) system with a well-defined Pd-Si order which has been supported by recent resonant elastic x-ray scattering (REXS) data.[10,11)] This order gives rise to two inequivalent rare earth sites leading to a complex magnetic structure as well as a generic phase diagram.[12)]

The rare-earth ions Dy^{3+} and Ho^{3+} with partly filled $4f^7$ shell have a strong spin–orbit coupling and are subject to crystal field (CF) effects. In their intermetallic compounds R_2PdSi_3, the electronic properties are governed by the CF effect and by RKKY exchange interactions.[13)] In Dy_2PdSi_3, magnetic order has been reported below 8 K with dominating AFM coupling in the basal plane and a ferromagnetic (FM) type magnetic coupling along the c-axis.[12)] The c-axis becomes the magnetic easy axis below ~25 K while above the a-axis is the easy one. In addition, giant magneto-resistance has been found in this compound.[4)] As for Ho_2PdSi_3, the c-axis is the magnetic easy direction below ~40 K.[12)] Well below T_N, at $T_2 = 2.3$ K, a possible spin reorientation has been reported.[14)] Sizeable magnetic anisotropy has been observed for both Dy_2PdSi_3 and Ho_2PdSi_3 and it may be expected that magnetic anomalies are associated with pronounced lattice changes.[15,16)] However, apart from a recent study on a Eu_2CuSi_3 single crystal,[17)] there is no investigation of anisotropic magneto-elastic effects for any member of this class of materials, let alone R_2PdSi_3 (R = Ho, Dy) which have the highest effective paramagnetic moment among all their analogues.[12)] In the present work, we investigate in detail the uniaxial lattice distortions induced by the magnetic transition and the CF effects as well as the influence of external magnetic fields on R_2PdSi_3 (R = Ho, Dy) single crystals. Our thermal expansion and magnetostriction data demonstrate pronounced coupling of structural, magnetic, and electron degrees of freedom and the data are used to construct and to complete the electronic phase diagrams for both compounds.

2. Experimental Methods

The growth of the R_2PdSi_3 (R = Ho, Dy) single crystals by a floating zone method is described in Ref. 18. In order to determine the uniaxial length changes of the crystals, two types of three-terminal capacitance dilatometers have been used which provided consistent results. Detailed information on the dilatometers are presented in Refs. 19, 20, and 21, respectively. The thermal expansion coefficient $\alpha_i = 1/L_i \cdot dL_i(T)/dT$ and the magnetostriction coefficient $\lambda_i = 1/L_i \cdot dL_i(H)/dH$ are derived from the length measurements upon variation of the temperature and of the magnetic field. Magnetic fields have been applied along the direction of the measured length changes. The specific heat was measured with the Physical Property Measurement System (PPMS) from Quantum Design by employing the relaxation method.

3. Thermal Expansion at $B = 0$ and Grüneisen Analysis

Figure 1(a) shows the uniaxial thermal expansion of

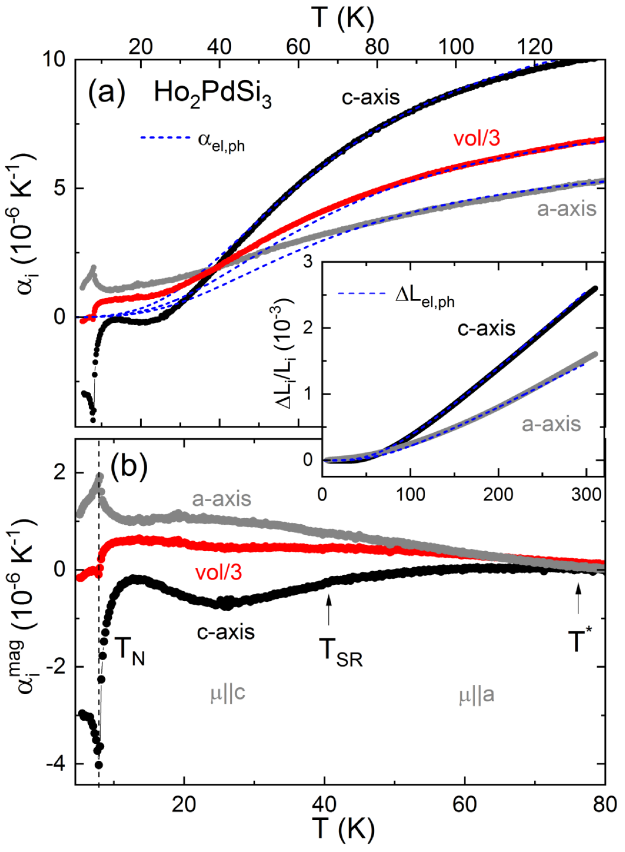

Fig. 1. (Color online) (a) Linear thermal expansion coefficients α of Ho_2PdSi_3 along the a-axis and the c-axis as well as the calculated 1/3 volume expansion (red). The inset shows the relative length changes $\Delta L/L$ and the blue dashed lines in both graphs show the fitted electron and phonon background $\alpha_{e,ph}$. (b) The background corrected thermal expansion $\alpha_i^{mag} = \alpha - \alpha_{e,ph}$ vs T in log scale. The vertical dashed line marks T_N. T^* signals the onset of anisotropy in α and the spin-reorientation temperature T_{SR} is taken from Ref. 12.

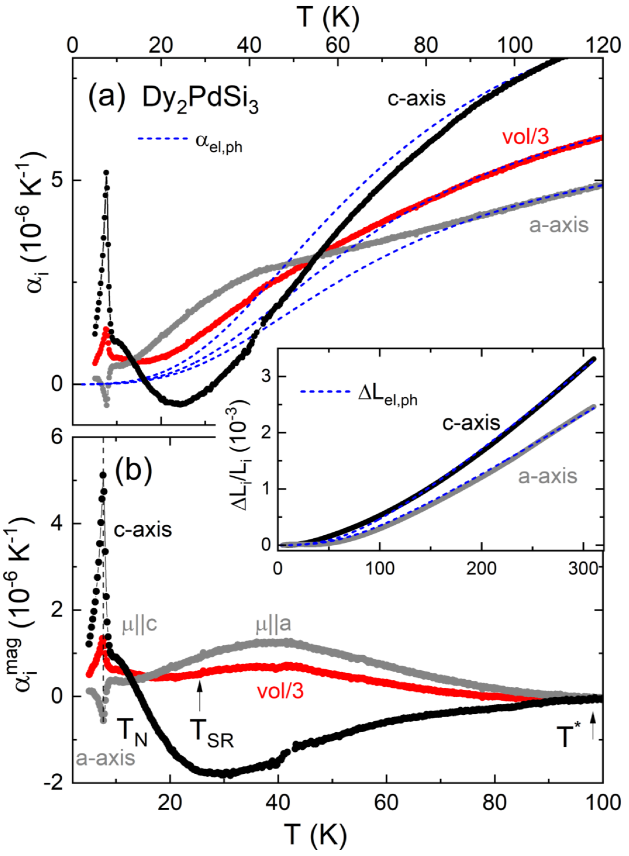

Fig. 2. (Color online) (a) Linear thermal expansion coefficients α of Dy_2PdSi_3 along the a-axis and the c-axis as well as the calculated 1/3 volume expansion. The inset shows the relative length changes $\Delta L/L$ and the blue dashed lines in both graphs show the fitted electron and phonon background $\alpha_{e,ph}$. (b) Background corrected thermal expansion $\alpha_i^{mag} = \alpha - \alpha_{e,ph}$ vs T in log scale. The vertical dashed line marks T_N. T^* signals the onset of anisotropy in α and the spin-reorientation temperature T_{SR} is taken from Ref. 12.

Ho_2PdSi_3 without external magnetic field. The uniaxial thermal expansion coefficients along both axes, α_a and α_c, as well as the volume thermal expansion coefficient α_v show pronounced anomalies at $T_N = 7.8(3)$ K indicating the onset of long-range antiferromagnetic order as supported by AC-susceptibility, magnetisation, and neutron data.[12,16] The anomalies in α are λ-shaped. They correspond to humps in the relative length changes indicating shrinking of the c-axis and increase of the a-axis at T_N upon cooling. The different signs of the anomalies imply opposite uniaxial pressure dependencies of T_N, i.e., $dT_N/dp_a > 0$, $dT_N/dp_c < 0$. In addition, the anomaly in α_v implies negative hydrostatic pressure dependence of T_N. As seen in the inset of Fig. 1(a), the overall length changes up to the room temperature are quite anisotropic, i.e., at $T = 300$ K, $\Delta L_c/L_c = 2.56 \cdot 10^{-3}$ is nearly 1.5 times larger than $\Delta L_a/L_a = 1.58 \cdot 10^{-3}$.

The dashed blue lines show fits of the electronic and phononic contribution to the thermal expansion coefficients α and to the length changes $\Delta L_i/L_i$ at high temperatures using the functions:[22]

$$\alpha_{e,ph} = \alpha_{el} + \alpha_{ph} \tag{1}$$

$$\approx K_1 T + K_2 D\left(\frac{\Theta}{T}\right), \tag{2}$$

and

$$\left.\frac{\Delta L}{L}\right|_{e,ph} = \left(\frac{\Delta L}{L}\right)_{el} + \left(\frac{\Delta L}{L}\right)_{ph} \tag{3}$$

$$\approx K_1 T^2 + K_2 T D\left(\frac{\Theta}{T}\right). \tag{4}$$

K_1 and K_2 are constants while $D(\Theta/T)$ denotes the Debye function with the Debye temperature Θ. Fitting the data with these equations yields estimates of the the electron and phonon background $\alpha_{e,ph}$ [blue dashed line in Fig. 1(a)], with the Debye temperature $\Theta = 284$ K. The magnetic and CF contributions α^{mag} shown in Fig. 1(b) are obtained by subtracting $\alpha_{e,ph}$ from the experimental data. For all axes, we find anisotropic α^{mag} up to about $T^* = 70(10)$ K while for $T > T^*$ the data are well described by the fits.

The thermal expansion coefficients α_a, α_c, and α_v of Dy_2PdSi_3 in zero field in Fig. 2(a) present similarly sharp anomalies associated with the onset of long-range order as for Ho_2PdSi_3. Again, the anomalies imply opposite uniaxial pressure dependencies which however differ from the ones in Ho_2PdSi_3: In Dy_2PdSi_3, the c-axis increases and the a-axis decrease upon the onset of long range AFM order. This implies $dT_N/dp_a < 0$ and $dT_N/dp_c > 0$ which is opposite as compared to Ho_2PdSi_3. In addition, the hydrostatic pressure dependence has a different sign than in Ho_2PdSi_3, i.e., applying hydrostatic pressure yields an increase of T_N in

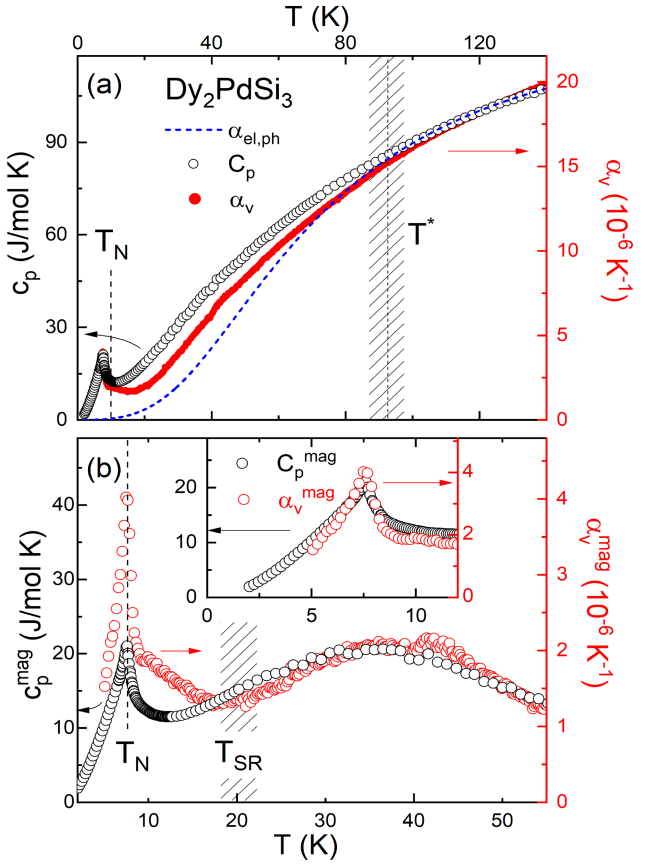

Fig. 3. (Color online) (a) Comparison between the volume thermal expansion coefficient α_v of Dy_2PdSi_3 and the heat capacity c_p. The dashed blue line shows the phonon background. T^* marks the onset of anisotropic contributions α^{mag}. (b) Scaling behavior of α^{mag} and the heat capacity c_p^{magn}. The dashed area indicates the spin-reorientation temperature T_{SR}. The inset shows the same data scaled with a Grüneisen ratio appropriate for $T < T_{SR}$ (see the text).

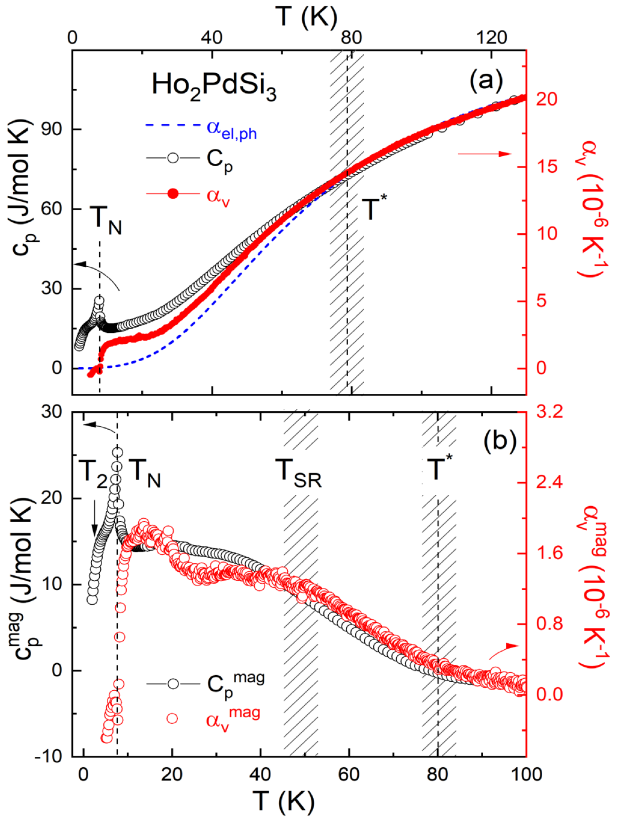

Fig. 4. (Color online) (a) Comparison between the volume thermal expansion coefficient α_v of Dy_2PdSi_3 and the heat capacity c_p. The dashed blue line shows the phonon background. T^* marks the onset of magnetic CF contributions. (b) Scaling behavior of α^{mag} and the heat capacity c_p^{magn}. T_N and T^* mark the onset of long-range and short-range magnetic order, T_{SR} the spin-reorientation temperature. T_2 is an additional feature as discussed in the text.

Dy_2PdSi_3. The anisotropy in the overall length changes $\Delta L_c/L_c = 2.46 \cdot 10^{-3}$ and $\Delta L_a/L_a = 3.33 \cdot 10^{-3}$ is a bit smaller than in Ho_2PdSi_3. Finally, applying the same procedure as described above for assessing $\alpha_{e,ph}$ yields $\Theta = 309\,\mathrm{K}$ and $T^* = 92(5)\,\mathrm{K}$. The resulting background corrected thermal expansion coefficients are shown in Fig. 2(b).

Further information is obtained by comparing the anomalous length and entropy changes. In the presence of one dominant energy scale ϵ the thermal expansion coefficient α and the heat capacity c_p are related by the Grüneisen relation

$$\Gamma = \frac{\alpha}{c_p} = \frac{1}{V_m}\frac{\partial \ln \epsilon}{\partial p}, \qquad (5)$$

where V_m is the molar volume. At T_N, Eq. (5) converts to $\Gamma = (T_N V_m)^{-1} \partial T_N/\partial p$.

The overall temperature dependence of the volume thermal expansion coefficient and the specific heat is shown in Fig. 3(a). The particular scaling used in the figure shows a constant ratio α_v/c_p above the temperature T_{SR}. Above T^*, both entropy and length changes are mainly phononic. This is confirmed by a fit to the experimental data using the same Debye temperature Θ for both α_v and c_p [dashed blue line in Fig. 3(a)]. The resulting specific heat contribution $c_p^{magn} = c_p - c_p^{ph}$ (with c_p^{ph} the phonon specific heat) agrees to a previous analysis of the low temperature specific heat.[23] c_p^{magn} shows a broad hump-like anomaly which we attribute to Schottky anomalies originating from the thermal population of the CF states. The anomalous thermal expansion and specific heat are displayed in Fig. 3(b), again with appropriate scaling. The data imply two regions of different Grüneisen scaling, i.e., $\Gamma(T > T_{SR}) = 1.5(3) * 10^{-7}\,\mathrm{J^{-1}\,mol}$ and $\Gamma(T < T_{SR}) = 1.9(1) * 10^{-7}\,\mathrm{J^{-1}\,mol}$.

The analogous analysis for Ho_2PdSi_3 is presented in Fig. 4. The data start deviating from the background at similar temperatures as in Dy_2PdSi_3. In contrast, however, there is no clear change in the Grüneisen ratio at T_{SR} but we find a rather temperature independent value of Γ down to nearly T_N. At lower temperatures, the scaling fails and the data proof negative hydrostatic pressure dependence of T_N. We also note a small hump in the specific heat at around $T_2 = 3.3\,\mathrm{K}$. It might be related to a squared-up magnetic structure appearing at 2.3 K.[4,14,16]

4. Thermal Expansion at $B \neq 0$ and Magnetostriction

In Fig. 5(a) the relative length changes $\Delta L_a/L_a(T)$ of Ho_2PdSi_3 under the influence of different magnetic fields are shown. In general, magnetic fields lead to larger thermal expansion in the measured temperature range $T \leq 60\,\mathrm{K}$. Note, that the magnetostriction data (blue data points) which were used to calibrate the field effect, at $T = 15\,\mathrm{K}$, fully agree to the $\Delta L(T)$ data at $B \neq 0$. Upon application of even small

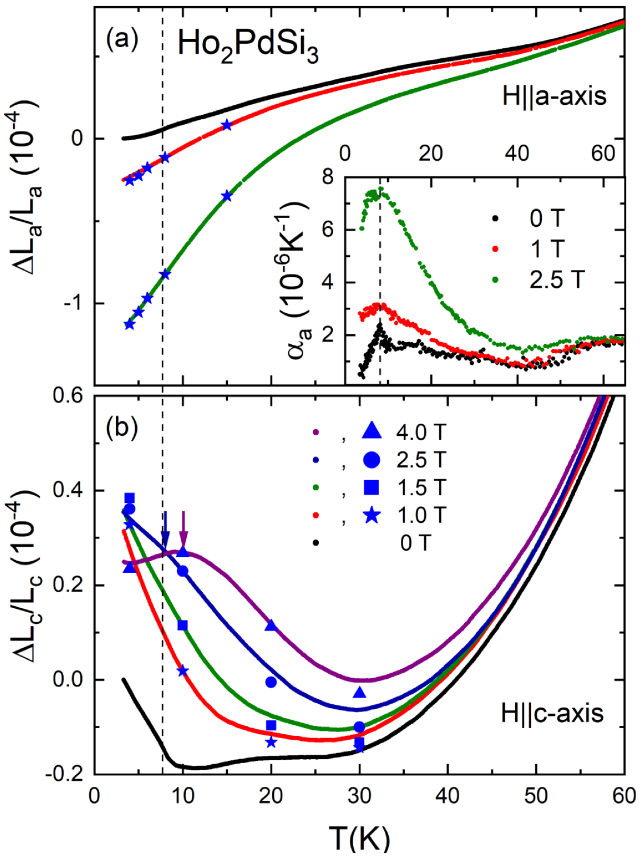

Fig. 5. (Color online) Relative length changes of Ho_2PdSi_3 in different external magnetic fields along (a) the a-axis and (b) the c-axis. The blue data points have been obtained by magnetostriction measurements and the vertical dashed line shows T_N ($B = 0$ T).

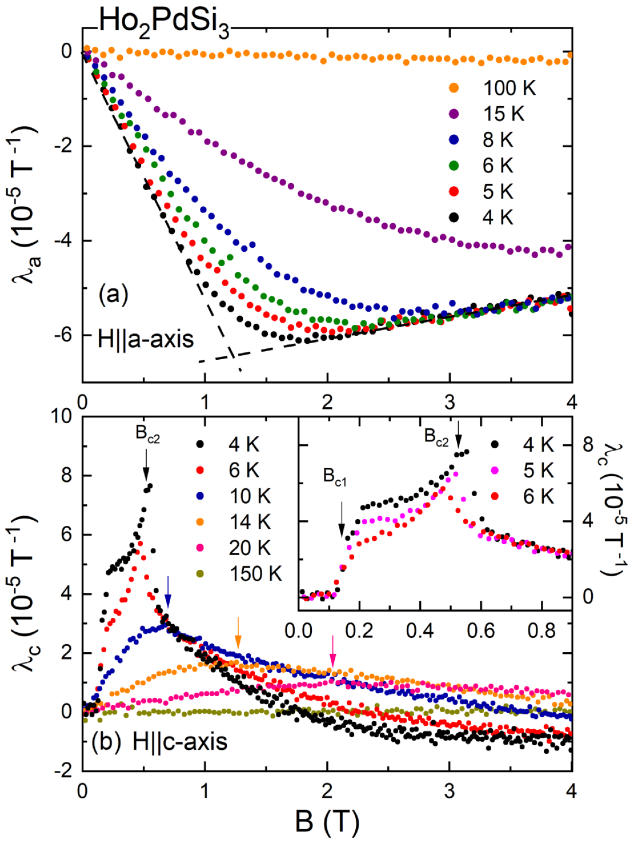

Fig. 6. (Color online) Linear magnetostriction coefficients (a) λ_a and (b) λ_c of Ho_2PdSi_3 for different temperatures. The dashed lines in (a) illustrate how the FiM to FIM′ phase boundary was extracted. The inset in (b) highlights the low-field region with B_{c1} and B_{c2} indicating the center of a step and a peak, respectively, in λ_c. The step-like anomalies B_{c1} are visible only at low temperature $T \leq 6$ K (insert of b).

magnetic fields, e.g., 1 T, the λ-shaped anomaly in α_a disappears in favor for a much larger broad hump which is associated with strongly increased overall length changes. Accordingly, the regime of negative thermal expansion along the c-axis which is restricted to $T \lesssim T_N$ at $B = 0$ extends to about 30 K at $B = 2.5$ T. This yields disappearance of the feature between 10 and 15 K in $\Delta L_a(B = 0)$ in favour of a concave feature with the minimum at ~30 K gradually showing up. Below T_N, the signal changes from negative ($B \leq 2.5$ T) to positive thermal expansion ($B = 4$ T). The associated hump in $L_c(T)$ evolving at $B \geq 2.5$ T agrees with a faint change of the AC-susceptibility indicating a phase boundary or crossover between two ferrimagnetic phases (FiM and FiM′, see Fig. 9) which microscopic origin is not yet clear.[16)]

Magnetostriction data on Ho_2PdSi_3 confirm the observed field dependence of the thermal expansion and enable to complete the phase diagram (Fig. 6). For $B \parallel a$, the sample length decreases for small magnetic fields and increases in the high field regime. Comparison with the phase diagram in Ref. 16 suggests that these changes signal a crossover within the ferrimagnetic (FiM) phase. For $B \parallel c$-axis, at $T = 4$ K, the magnetostriction coefficient λ_c shows a sharp peak and a step-like anomaly which are marked as B_{c2} and B_{c1} in Fig. S1(b). B_{c2} is attributed to the transition from the AFM to the FiM phase.[16)] Upon heating, B_{c2} shifts to higher fields and smears out so that it can only be extracted for $T \leq 20$ K. In addition, at $T \leq 6$ K, the step-like anomaly B_{c1} is observed as a kind of shoulder prior to the AFM-FiM transition at B_{c2}. The critical field B_{c1} is extracted as the middle of the step. Below B_{c1}, the magnetostriction is nearly zero. At high temperature, both λ_a and λ_c imply negligible magnetostriction.

The overall field dependence of the thermal expansion of Dy_2PdSi_3 is similar to what is found in Ho_2PdSi_3: The data in Fig. 7(a) confirm a strong contraction of the sample for $B \parallel a$. Again, the signatures of the phase transition and of the ordered phase are suppressed by the magnetic field. The presence of significant magnetostrictive effects extends up to larger temperatures as compared to Ho_2PdSi_3 which agrees to the larger region of anomalous length changes suggested by our analysis of the zero field thermal expansion coefficient (see Figs. 1 and 2). The application of magnetic fields along the c-axis leads to an expansion of the sample [Fig. 7(b)]. The size of the peak in α_c at T_N gradually vanishes upon increasing the magnetic field and it is absent at $B > 1$ T. However, even at $B = 5$ T there is still a kink in α_c. The right shoulder in α_c is suppressed and the minimum around 25 K becomes more pronounced. This can be seen more clearly in the magnetostriction coefficient λ_c [Fig. 8(b)]. It exhibits a peak in the ordered phase which significantly broadens and shifts to higher field upon heating above T_N. The position of the minimum suggests that it corresponds to the onset of the FiM region. An associated anomaly B_{a1} is also seen in λ_a in Fig. 8(a) where the distinct minima are marked by arrows.

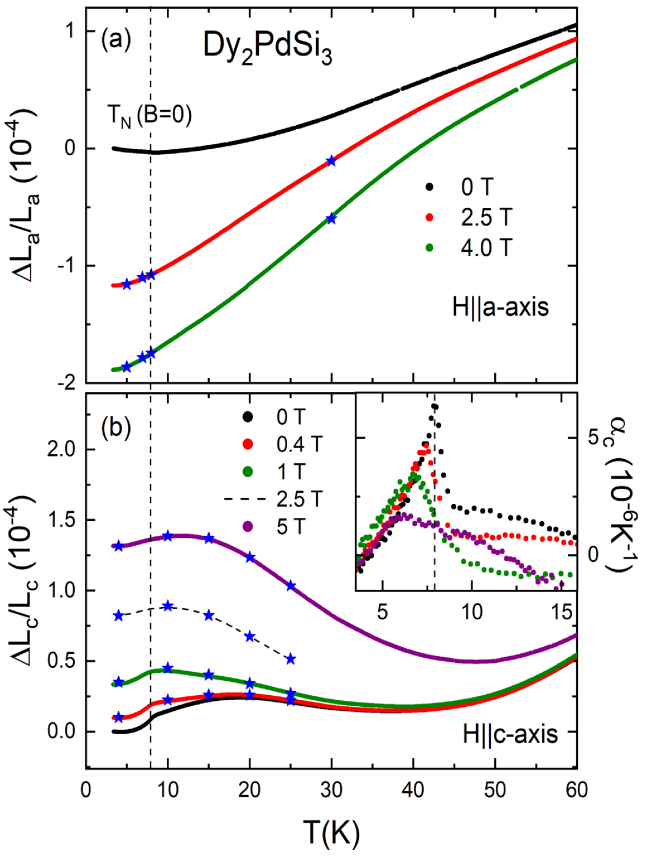

Fig. 7. (Color online) Relative length changes of Ho_2PdSi_3 in different external magnetic fields along (a) the a-axis and (b) the c-axis. The vertical dashed line shows T_N ($B = 0$ T). The blue data points have been obtained by magnetostriction measurements and the dashed line serves as a guide to the eye for the 2.5 T curve. The inset of (b) shows the derivative α_c of the data in (b).

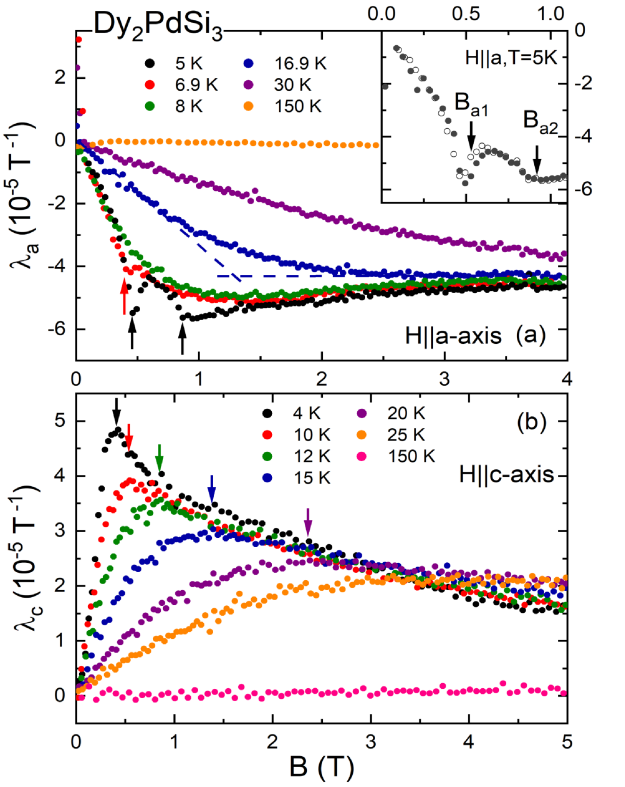

Fig. 8. (Color online) Linear magnetostriction coefficients (a) λ_a and (b) λ_c of Dy_2PdSi_3 for different temperatures. The dashed lines in (a) illustrate how the phase boundary was extracted. The insert is the enlarged view of data at $T = 5$ K at field below 2 T. The arrows mark the critical fields B_{a1}, B_{a2}, and B_c.

Somehow similar to Ho_2PdSi_3, an additional transition point shows up at B_{a2} which may suggest a spin reorientation process. The fact that it only appears for magnetic fields parallel to the easy axes both for Dy_2PdSi_3 and Ho_2PdSi_3 confirms its magnetic origin. In addition, the magnetostriction data again suggest two regions with different slopes which crossover shifts towards higher fields upon heating. As the curves gradually flatten for higher temperatures, only the measurements up to $T = 16.9$ K are considered for determining the associated boundary. In this temperature regime, magnetostriction becomes independent on the temperature at $B \parallel a \gtrsim 3$ T where magnetisation curves show the change of the easy axis from the c- to the a-axis.[4,16)]

5. Magnetic Phase Diagrams and Discussion

Figure 9 presents the magnetic phase diagram of Ho_2PdSi_3, summarizing the results of the specific heat, thermal expansion and magnetostriction studies as well as the susceptibility anomalies from Ref. 16. The magnetic phase diagram of Dy_2PdSi_3 shown in Fig. 10 has been derived in the same way. The data suggest a similar, yet more simple phase diagram with AFM, PM, and FiM phases. Note, that no signature of spin reorientation, at $B = 0$, is visible in the data nor has been reported in the literature. In both compounds, the obtained phase diagrams differ from the generic one suggested for the R_2PdSi_3 compounds.[12)] The main results for both compounds are discussed in the following.

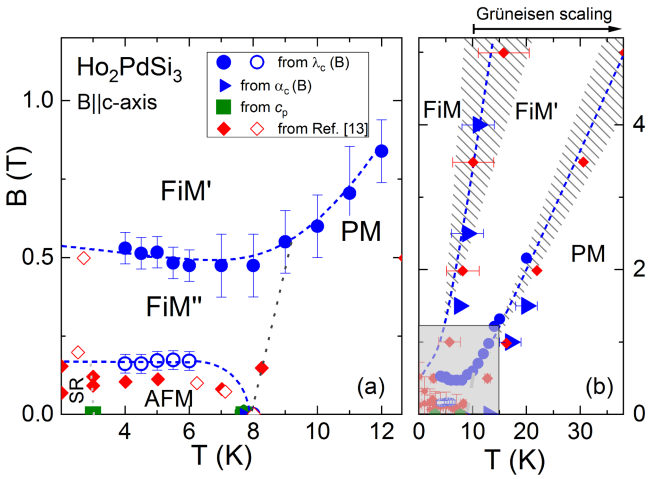

Fig. 9. (Color online) Magnetic phase diagram of Ho_2PdSi_3 from specific heat (squares), thermal expansion (circles), and magnetostriction data (triangles). Solid and hollow diamonds show data from Ref. 16. AFM, SR, FiM/Fim′/FiM″, and PM label antiferromagnetic, spin-reoriented, ferrimagnetic, and paramagnetic phases. The shaded region in (b) shows the (B, T)-range covered in (a).

(1) Both phase diagrams show long-range AFM order appearing at similar temperatures T_N. At T_N, the thermal expansion data of Ho_2PdSi_3 imply opposite uniaxial pressure dependencies, i.e., $dT_N/dp_a > 0$, $dT_N/dp_c < 0$, and the hydrostatic pressure dependence is negative. For Dy_2PdSi_3, the uniaxial pressure dependencies are opposite, i.e.,

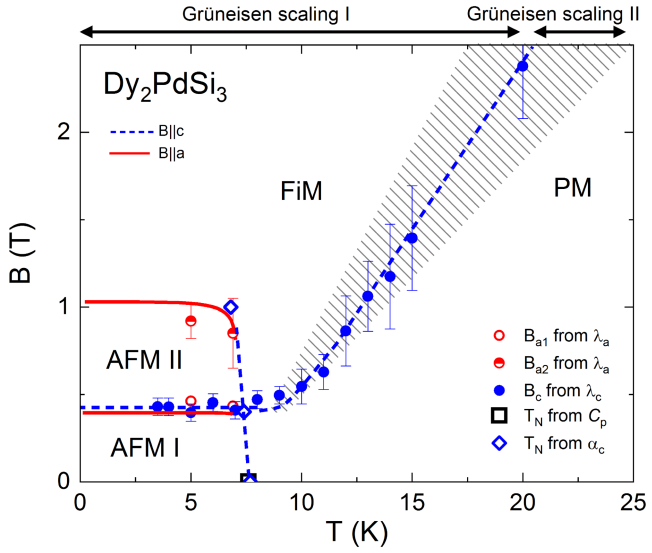

Fig. 10. (Color online) Magnetic phase diagram of Dy_2PdSi_3 from specific heat (square), thermal expansion (empty diamonds), and magnetostriction (circles) data. AFM I/II, FiM, and PM label antiferromagnetic, ferrimagnetic, and paramagnetic phases.

$dT_N/dp_a < 0$ and $dT_N/dp_c > 0$, and the hydrostatic pressure dependence is positive. This qualitatively different pressure dependence implies that, at T_N, different ground states evolve in Ho_2PdSi_3 and Dy_2PdSi_3 which is confirmed by neutron diffraction.[12)]

(2) At rather high temperature $T^* > 10 \cdot T_N$, anisotropy of the uniaxial thermal expansion as well as the presence of magnetic CF contributions to the thermal expansion and the specific heat signal depopulation of the crystal-field levels. Note, that the magnetic susceptibility follows a Curie–Weiss law down to around 50 K in Ho_2PdSi_3 and only down to around 80 K in Dy_2PdSi_3.[12)] The easy magnetic axis at high temperatures is along the a-direction which is consistent with the negative sign of the Stevens factors.[24)] It rotates towards the c-axis at around $T_{SR} \approx 40$ K (Ho_2PdSi_3) and 25 K (Dy_2PdSi_3) (see Ref. 12) which underlines the subtle interplay between crystal field effects and spin–orbit coupling.

(3) In Ho_2PdSi_3, the hydrostatic pressure dependence at T_N is negative and does not agree to the positive Grüneisen parameter at higher temperatures. This observation demonstrates the different nature of the underlying entropy and length changes, i.e., Schottky-type crystal field effects at high temperatures and magnetic ordering around T_N. In Dy_2PdSi_3, Grüneisen scaling is valid with a single Grüneisen parameter in the regime $T_{SR} \leq T \leq T^*$ and is violated at $12\,K \leq T \leq T_{SR}$. We conclude that in this temperature regime there are both the Schottky anomaly and AFM fluctuations present while the latter dominate only below 12 K, yielding another single, i.e., magnetic Grüneisen parameter. This observation implies that short-range AFM correlations at $T < 12$ K and the AFM phase have the same hydrostatic pressure dependence. We conclude the common nature of AFM short- and long-range order for Ho_2PdSi_3.

(4) In Ho_2PdSi_3, AFM to FiM″ is a metamagnetic transition driven by $B \parallel c$-axis.[12)] The jump of magnetisation $\Delta M_{c1} \approx 5$–$6\,\mu_B$/Ho (see Ref. 12), at B_{c1}, is associated with a jump of the magnetostriction coefficient $\Delta\lambda_c = 5.0(5) \cdot 10^{-5}$/T. In contrast, the magnetostriction peak at B_{c2} is not associated with a clear anomaly in M vs B and the hysteresis of the magnetisation is not resembled by the magnetostriction. Both transitions at B_{c1} and B_{c2} are observed for B parallel to the easy c-axis only. The fact that the slope of the phase boundary is very small, i.e., $dB_{c1}/dT = -\Delta S_{c1}/\Delta M_{c1} \approx 0$, implies that there are no large entropy changes ΔS_{c1} at the metamagnetic transition AFM to FiM″. The same holds for AFM I to AFM II in Dy_2PdSi_3. In Ho_2PdSi_3, within the error bars, the phase boundaries $B_{a1}(T)$ and $B_{c2}(T)$ agree to the PM, FiM, and FiM′ phases proposed in Ref. 16. However, the peak in λ_c at B_{c2} signals the presence of the yet unknown region FiM″. Similar to $B_{c1}(T)$, B_{c2} appears for B parallel to the easy c-axis but there is no clear difference of magnetisation between FiM″ and FiM′.[12)]

(5) The evolution of FiM′ to FiM in Ho_2PdSi_3 yields shrinking of the sample. The associated anomaly may either signal a crossover or a continuous transition. The positive slope of the boundary implies larger magnetisation in the FiM regime. Magnetostriction is rather temperature independent in the FiM phase.

(6) In general, magnetic fields $B \parallel a$-axis yield shrinking of the a-axis while $B \parallel c$ increases the c-axis. This observation holds for both Ho_2PdSi_3 and Dy_2PdSi_3 and high temperatures. We attribute it to crystal-field effects and the alignment of magnetic moments along a. This is consistent to the fact that spin-reorientation at T_{SR} causes decrease of α_a. A similar consistency holds for the fact that applying $B \parallel c$-axis increases the c-axis.

(7) Magnetic fields applied along the easy magnetic axes align a ferromagnetic moment present in Dy_2PdSi_3 while there is a AFM phase in Ho_2PdSi_3 which undergoes a metamagnetic transition at finite field. The hysteresis in M vs B which in Dy_2PdSi_3 is centered around $B = 0$ for both axes is restricted to B_{c1} in Ho_2PdSi_3 which further emphasizes the different nature of AFM ground states in both systems. In contrast, the hysteresis in $L(B)$ in Dy_2PdSi_3 is restricted to a small region around B_{a1} and is clearly different from the hysteresis in $M(B)$. In particular, B_{a1} is not observed in the magnetisation.[4,12)]

6. Summary

In conclusion, we report detailed studies on the heat capacity, the thermal expansion and the magnetostriction of intermetallic compounds Dy_2PdSi_3 and Ho_2PdSi_3. The opposite signs of the thermal expansion anomalies at T_N show opposite pressure dependencies, thus revealing the different nature of the magnetic ground states in both materials. In both compounds, there are pronounced entropy and anisotropic length changes up to more than $10 \cdot T_N$ which are attributed to Schottky-type crystal field effects. Since the Grüneisen ratio changes with temperature we conclude that an interplay of different degrees of freedom is driving the observed anomalous length and entropy changes. Our data enable to construct the electronic phase diagrams including observation of yet unknown intermediate antiferromagnetic (Dy_2PdSi_3) and ferrimagnetic (Ho_2PdSi_3) regions evolving upon application of external magnetic fields. In summary, both the data analysis and the phase diagrams demonstrate the delicate balance and relation of CF effects and magnetic exchange interactions.

Acknowledgements L.W. thanks the support of Deutsche Forschungsgemeinschaft (DFG) through Grant No. WA4313/1-1. Two authors (H.B., W.L.) would like to thank G. Behr (†) for his support in crystal growth. M.A. thanks the support of DFG via Grant No. MO3014/1-1. CDC acknowledges financial support by the National Natural Science Foundation of China Grant No. 51471135, the National Key Research and Development Program of China under contract No. 2016YFB1100101, and Shaanxi International Cooperation Program. R.K. gratefully acknowledges fellowship of the Marsilius Kolleg Heidelberg.

*liran.wang@kip.uni-heidleberg.de
†Present address: Lyman Laboratory of Physics, Harvard University, Cambridge, Massachusetts 02138, U.S.A.
‡ruediger.klingeler@kip.uni-heidelberg.de

1) S. Majumdar and E. V. Sampathkumaran, Phys. Rev. B **63**, 172407 (2001).
2) T. Yamamura, D. Li, and Y. Shiokawa, Phys. B: Condens. Matter **329–333**, 559 (2003).
3) B. Chevalier, R. Pöttgen, B. Darriet, P. Gravereau, and J. Etourneau, J. Alloys Compd. **233**, 150 (1996).
4) S. Majumdar, H. Bitterlich, G. Behr, W. Löser, P. Paulose, and E. Sampathkumaran, Phys. Rev. B **64**, 012418 (2001).
5) M. Szlawska and D. Kaczorowski, Phys. Rev. B **85**, 134423 (2012).
6) Z. J. Mo, J. Shen, X. Q. Gao, Y. Liu, C. C. Tang, J. F. Wu, F. X. Hu, J. R. Sun, and B. G. Shen, J. Alloys Compd. **626**, 145 (2015).
7) Z. J. Mo, J. Shen, L. Q. Yan, X. Q. Gao, C. C. Tang, J. F. Wu, J. R. Sun, and B. G. Shen, J. Alloys Compd. **618**, 512 (2015).
8) A. Raman, Naturwissenschaften **54**, 560 (1967).
9) A. Szytuła, M. Hofmann, B. Penc, M. Ślaski, S. Majumdar, E. Sampathkumaran, and A. Zygmunt, J. Magn. Magn. Mater. **202**, 365 (1999).
10) F. Tang, M. Frontzek, J. Dshemuchadse, T. Leisegang, M. Zschornak, R. Mietrach, J.-U. Hoffmann, W. Löser, S. Gemming, D. C. Meyer, and M. Loewenhaupt, Phys. Rev. B **84**, 104105 (2011).
11) M. Nentwich, M. Zschornak, C. Richter, D. Novikov, and D. C. Meyer, J. Phys.: Condens. Matter **28**, 066002 (2016).
12) M. Frontzek, Ph.D. Thesis (2009).
13) J. Jensen and A. R. Mackintosh, *Rare Earth Magnetism* (Clarendon Press, Oxford, U.K., 1991).
14) E. V. Sampathkumaran, H. Bitterlich, K. K. Iyer, W. Löser, and G. Behr, Phys. Rev. B **66**, 052409 (2002).
15) S. Nimori and D. Li, J. Phys. Soc. Jpn. **75**, 195 (2006).
16) M. Frontzek, F. Tang, P. Link, A. Schneidewind, J.-U. Hoffman, J.-M. Mignot, and M. Loewenhaupt, Phys. Rev. B **82**, 174401 (2010).
17) L. Wang, L. Wallbaum, C. Koo, C. D. Cao, W. Löser, and R. Klingeler, arXiv:1702.00705.
18) G. Graw, H. Bitterlich, W. Löser, G. Behr, J. Fink, and L. Schultz, J. Alloys Compd. **308**, 193 (2000).
19) M. Rotter, H. Müller, E. Gratz, M. Dörr, and M. Loewenhaupt, Rev. Sci. Instrum. **69**, 2742 (1998).
20) L. Wang, U. Köhler, N. Leps, A. Kondrat, M. Nale, A. Gasparini, A. de Visser, G. Behr, C. Hess, R. Klingeler, and B. Büchner, Phys. Rev. B **80**, 094512 (2009).
21) C. Meingast, B. Blank, H. Bürkle, B. Obst, T. Wolf, H. Wühl, V. Selvamanickam, and K. Salama, Phys. Rev. B **41**, 11299 (1990).
22) E. Gratz and A. Lindbaum, J. Magn. Magn. Mater. **137**, 115 (1994).
23) R. Mallik, E. Sampathkumaran, and P. Paulose, Solid State Commun. **106**, 169 (1998).
24) M. Hutchings, Solid State Phys. **16**, 227 (1964).